




Polar inelastic profiles in fast-atom diffraction at surfaces

Peng Pan , Maxime Debiossac , and Philippe Roncin 

Université Paris-Saclay, CNRS, Institut des Sciences Moléculaires d'Orsay, 91405 Orsay, France



(Received 30 August 2021; accepted 1 October 2021; published 19 October 2021)

Elastic diffraction of fast atoms at crystal surfaces under grazing incidence $\theta \approx 1^\circ$ has strong similarities with atomic diffraction at thermal energies discovered almost hundred years ago. Here, we focus on the polar scattering profile, which does not exhibit diffraction features but shows well-defined elastic and inelastic components that are found to be essentially independent of the crystallographic axis. The width σ_θ of the inelastic component is very sensitive to the weak attractive forces responsible for the physisorption. This effect is visible on an energy range almost ten times larger than the depth D of the physisorption well. Experimental data are analyzed using a binary collision model with a Morse potential where the width σ_θ of the scattering profile is connected to the classical energy loss and is governed by the surface stiffness, defined as the logarithmic derivative of the interaction potential along the surface normal. The main outcome is that the weak attractive forces make the mean surface potential almost twice harder at low energy.

DOI: [10.1103/PhysRevB.104.165415](https://doi.org/10.1103/PhysRevB.104.165415)

I. INTRODUCTION

Grazing incidence fast atom diffraction at crystal surfaces (GIFAD or FAD) uses atoms in the keV energy range at incidence angles around 1° . When the surface coherence permits, a rich diffraction pattern can be obtained as once, as sketched in Fig. 1. This grazing geometry is the same as that of reflection high-energy electron diffraction (RHEED) leaving the volume above the surface free for evaporation cells. Similar to RHEED, GIFAD has shown pronounced intensity oscillation in the case of a layer by layer growth of GaAs/GaAs. However, in GIFAD, due to the absence of any penetration below the topmost layer, the oscillations maxima always correspond to a complete layer whatever the projectile energy, angle of incidence or crystallographic direction [1]. Before or after growth, the GIFAD elastic diffraction pattern is not only a very detailed fingerprint of the surface crystalline order, it is also a quantitative measure easily interpreted in terms of topology. It can be seen as a reciprocal space, atomic force microscope with a perfect tip made of a single helium atom. This offers high resolution [2,3], simple semiquantitative interpretation [4] and, when compared with exact scattering code, a parameter free accuracy [3,5]. As will be detailed in Sec. III A, the movement perpendicular to the probed crystallographic axis (x in Fig. 1) is strongly decoupled from the fast one parallel to the x axis so that the effective energy for elastic diffraction is $E_\perp = E \sin^2 \theta_i$ where E is the total projectile energy and $\theta_i \approx \sin \theta_i$ is the grazing angle of incidence. Using a simple optical model of a hard corrugated wall, the diffraction pattern is a Fourier transform of the equipotential surface at the energy E_\perp as sketched in blue on Fig. 1.

In this paper, we discuss a complementary aspect, the probability for a projectile atom to be deflected away from

a Bragg angle. More precisely, the inelastic polar scattering profile or angular distribution $P(\theta)$ defining the probability for the projectile to be deflected by an angle θ different from the specular angle. It does not display any diffraction feature, but our results below suggest that it is sensitive to the stiffness of the mean surface potential at the distance z_t where the projectile velocity towards the surface changes sign. More precisely, the stiffness is represented by the logarithmic derivative $-V'/V$ at the turning point z_t . For a purely repulsive mean planar potential $V(z) \propto e^{-\Gamma z}$, the stiffness is simply Γ and determines the number N of binary collisions taking place along the trajectory [6–8] as well as the momentum δp transferred to each encountered surface atom since quasispecular reflection implies that $N\delta p \sim 2k_{iz}$. In practice, weak van der Waals attractive forces generate a shallow potential well characterized by a depth D of a few meV only for hardly polarisable projectiles such as helium or neon. The purely repulsive model was expected to remain valid as soon as the perpendicular energy E_\perp is much larger than the depth D . This naive simplification was ruled out recently in a combined experimental and theoretical study using neon atoms [5]. This specific aspect is analyzed here in detail with different crystal orientations and different projectiles. We show that the dominant effect of the attractive forces on the inelastic scattering profile is to modify significantly the stiffness of the potential energy surface around the turning point z_t of the trajectory. An analytic model using the simple Morse potentials to link the observed data to the depth D on a broader energy range is presented.

The paper is structured as follows: Section II presents experimental data recorded with helium and neon projectiles on a LiF crystal surface at room temperature (except for Fig. 4 recorded at -93°C). The image transformation used to isolate the elastic and inelastic polar scattering profiles is

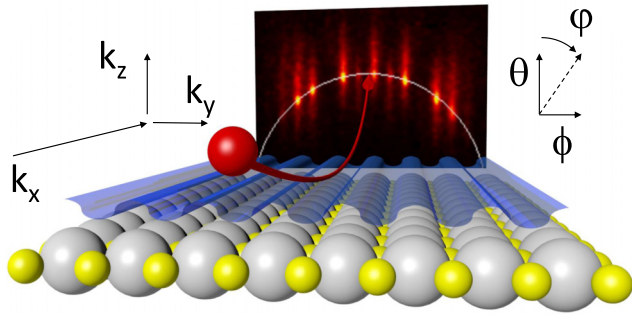


FIG. 1. Schematic view of the grazing scattering geometry. The image in the background is the diffraction pattern of 500 eV neon atoms at $\theta_i = 0.42^\circ$ impinging on LiF. The white line where bright spots are observed represents the Laue circle of energy conservation corresponding to elastic diffraction. Inelastic diffraction extends below and above the Laue circle.

detailed, and within the explored conditions, these are found to be independent of the probed crystallographic axis. A data reduction procedure is presented to extract four numbers and their evolution with the projectile energy and angle of incidence.

Section III briefly recalls properties of elastic and inelastic diffraction in GIFAD and simple models developed to retrieve physical properties of the system such as the shape of the electronic density profile, the depth of the attractive well, the surface stiffness, and the thermal movement of surface atoms. The model is adapted to take into account the role of the attractive part of the mean planar interaction potential drastically improving the agreement with experiment. Section IV addresses the gaps of the model trying to draw perspectives for future work.

II. GIFAD DIFFRACTION PATTERNS, THE POLAR PROFILE

A GIFAD setup is sketched in Fig. 1, see e.g., Refs. [5,9] for more details. It mainly consists of an atomic beam, incident at grazing incidence on a crystal surface and an imaging detector [10–12] located ≈ 1 m downstream to record the grazingly scattered atoms. The atom beam is formed by charged exchange from a parent ion beam directly extracted at the desired energy from a standard ion source. The critical part here is to reduce the divergence of the atomic beam below $1/100$ of a degree, and in our case, this is achieved by two diaphragms having a diameter typically less than $100 \mu\text{m}$ separated by half a meter. The raw diffraction images, such as the one in Fig. 1 and Fig. 2(d) show bright spots having a similar dimension to that of the primary atom beam and located on a circle. In these figures, the z direction is normal to the surface plane, and the x, y directions on the surface plane are defined as parallel and perpendicular to the low index direction probed respectively, see Fig. 1. The large distance to the detector together with the narrow beam profile allows direct conversion of the impact location to the scattering angles or to projectile momentum $\vec{k}_\perp(k_y, k_z)$ perpendicular to the x axis. As suggested by Fig. 1, GIFAD can be viewed as the diffraction of the fast atom

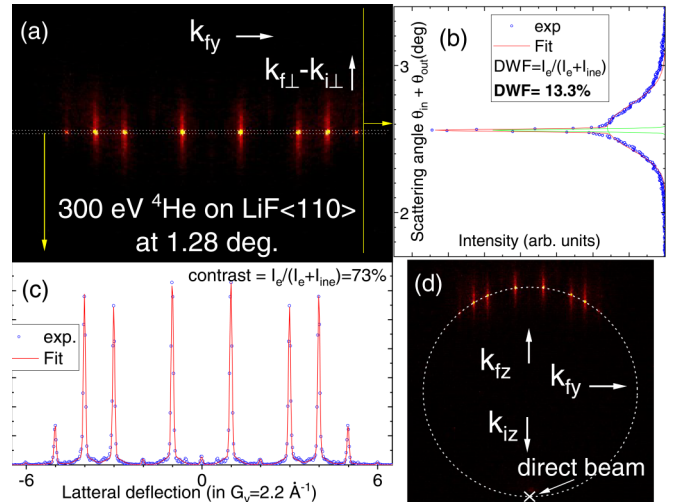


FIG. 2. (a) Quasipolar transform of the raw diffraction image in panel (d). Panel (b) corresponds to a full projection onto the vertical axis producing the polar scattering profile. Experimental data are fitted using the sum of a narrow Gaussian and a broad log-normal profile. Panel (c) corresponds to the intensity in a narrow horizontal band centered on the specular reflection.

wave by the well-aligned rows of surface atoms separated by a distance a_y so that diffraction only occurs along the y direction with an associated Bragg angle $\phi_B = G_y/k$ with $G_y = 2\pi/a_y$.

Before or after any measurement, the exact location and shape of the direct beam are recorded by removing the target surface from the primary atomic beam. The native images correspond to (k_y, k_z) coordinates, these are transformed into (k_y, k_\perp) using a polar transformation where k_\perp is the diameter of the circle hosting this point (k_y, k_z) , the direct beam and having its center on the scattering plane, i.e., on the line joining the specular spot to the direct beam location (see [13] for details). The derived diameter corresponds to an effective scattering angle $|\vec{k}_{f\perp} - \vec{k}_{i\perp}|$. The condition $|\vec{k}_{i\perp}| = |\vec{k}_{f\perp}|$ corresponds to the energy conservation and defines the Laue circle where the elastic spots are located. The transformed images in Figs. 2(a) and 3(a) show the well-aligned elastically diffracted spots. The associated intensity concentrated on a narrow horizontal stripe is plotted in Figs. 2(c) and 3(c) showing well-resolved peaks evenly separated by multiples of G_y . Away from this line of energy conservation, clear signs of inelastic diffraction remain visible in the form of vertical stripes extending on both sides as in Fig. 2(a), or preferentially upward or downward as in Figs. 3(a) and 3(d). The intensity integrated along the y direction produces the polar scattering profiles in Figs. 2(b) and 3(b) where the diffraction features have disappeared. These polar scattering profiles visible in Fig. 2(b) and 3(b) are well-fitted by the sum of a narrow Gaussian profile, *a priori* identical to those visible in Figs. 2(c) and 3(c) on top of a broader log-normal distribution. This log-normal profile (1) was empirically adopted as a data-reduction procedure [14] because it was found to reproduce the asymmetry of the scattering profile in the classical scattering regime [15,16] when diffraction was not considered. It was also observed in quantum Monte Carlo [17] or semiclassical

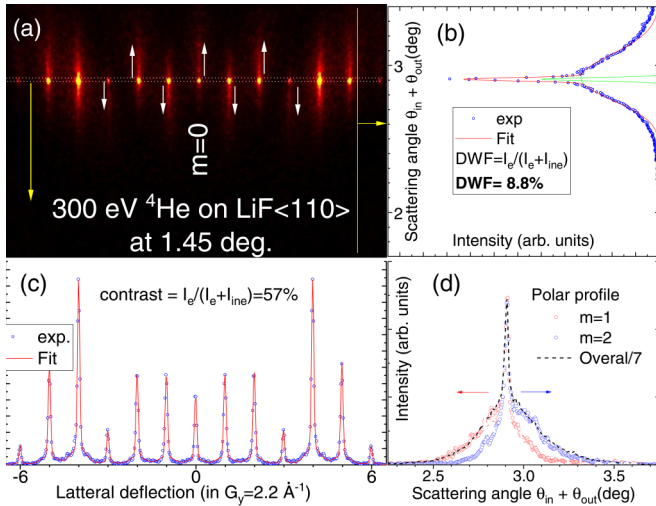


FIG. 3. Same as Fig. 2 with identical scales but with an angle of incidence $\theta_i = 1.45^\circ$ corresponding to an energy $E_\perp = 192$ meV. Panel (d) now displays the polar scattering profile associated with the $m = \pm 1$ and $m = \pm 2$ diffraction orders showing an inelastic component pointing mainly towards low (●) or large (●) scattering angles, respectively.

[18] and classical [15] approaches of scattering or inelastic diffraction. In the present context the adjustment has also the effect of rejecting the intensity observed far from the specular angle, which is believed to be dominated by surface defects [19], see e.g., Figs. 2(b), 3(b), and 4. For small values of $w \leq 0.1$ as measured here, $\sigma_{\text{ine}}^2 \approx w^2 \theta_m^2$, so that w is simply the relative width $w \approx \sigma_{\text{ine}}/\theta_m$, where θ_m is the median value

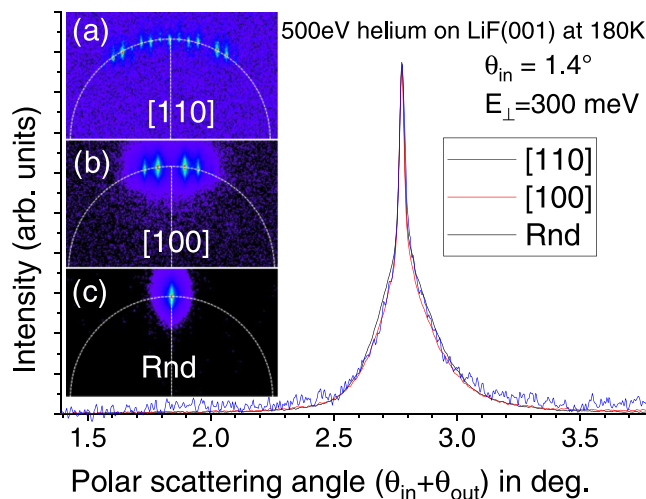


FIG. 4. [(a)–(c)] Raw diffraction images of 500 eV helium incident at 1.4° on LiF at 180 K oriented along the [110], [100], and random direction, respectively. The resulting polar scattering profiles are almost identical, showing a narrow elastic peak at $\theta_{\text{out}} = \theta_{\text{in}}$ on top of a quasi-log-normal inelastic profile having a relative width $w = \sigma_\theta/\theta \approx 0.042 \pm 0.002$.

very close to the specular scattering angle $\theta_s = 2\theta_{\text{in}}$.

$$LN[\theta_m; w](\theta) = \frac{A}{w\theta\sqrt{2\pi}} \exp\left(\frac{-\left(\ln\frac{\theta}{\theta_m}\right)^2}{2w^2}\right)$$

with a variance $\sigma_{\text{ine}}^2 = e^{w^2}(e^{w^2} - 1)\theta_m^2$

$$\text{and reversely } w = \left(\ln\frac{1 + \sqrt{1 + 4\sigma_{\text{ine}}^2/\theta_m^2}}{2}\right)^{1/2} \quad (1)$$

Figure 4 shows three almost identical polar scattering profiles recorded at the same incidence angle but along three different crystal orientation. This suggests that, for $E_\perp < 1$ eV where the distance to the surface is probably more than 2 \AA , the magnitude of the momentum exchanged along z is not very sensitive to the exact crystallographic direction as also suggested in Ref. [20] when investigating the azimuthal line profile of inelastic diffraction peaks.

Four independent pieces of information can be extracted from the analysis of these polar scattering distributions as a sum of Gaussian and log-normal profiles:

- (A) The intensity ratio of these profiles.
- (B) The elastic scattering width σ_e of the Gaussian profile.
- (C) The inelastic scattering width w of the log-normal inelastic profile (or its standard deviation σ_{ine}).
- (D) The shift $\delta\theta = \theta_m - \theta_s$, between the inelastic and elastic polar profiles.

These four items are first presented separately, and will be discussed together after a few theoretical considerations.

A. The elastic diffraction ratio

The ratio of elastic scattering is considered to be a direct measure of the Debye-Waller factor describing the overall coherence when the projectile wave is scattered by a single impact, e.g., x-ray, neutron, and atoms at thermal energies (TEAS, see e.g., [21] for a review) on thermally displaced surface atoms at a temperature T : $I(T)/I_0 = e^{-2W(T)}$ with $2W(T) = \langle (\bar{u} \cdot \Delta \vec{k})^2 \rangle_T$, where \bar{u} describe the displacement vector of surface atoms. Considering only displacement u_z along the z direction and after averaging at a temperature T , $2W = \langle u_z^2 \rangle_T \cdot (\Delta k_z)^2$, where $2W$ can be seen as the square of the phase spread due to the dispersion of the position u_z providing a geometric interpretation of the Debye-Waller factor. In TEAS, which was found to be in close analogy with GIFAD for elastic diffraction, the stiffness of the interaction potential does not enter the DWF. This is because the projectile mainly interacts with a single surface atom and therefore the momentum $\Delta k \sim 2k_i$ will eventually be exchanged with this atom, the stiffness only governs the time $\tau \approx 1/\Gamma v$ needed to exchange this momentum. Under grazing incidence, the same time $\tau \approx 1/\Gamma v_\perp$ is needed to bounce off the surface by exchanging the same momentum $2k_\perp$. However, this time τ now governs the distance $L = v_\parallel \tau$ spanned during this time and therefore determines the mean number of lattice sites $N \approx L/a$ that will be involved in the specular reflection where $v_\parallel = v_o \cos \theta_{\text{in}}$ and $v_\perp = v_o \sin \theta_{\text{in}}$ are the velocity component parallel and perpendicular to the surface. Assuming that these N sites participate equally to the momentum reversal from

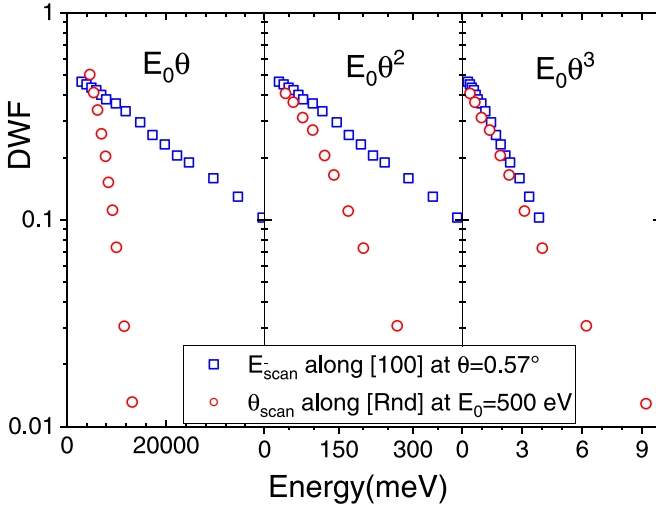


FIG. 5. The DWF, measured as the relative intensity of elastic diffraction of He projectiles on LiF during an E_{scan} (\square) or a θ_{scan} (\circ) are reported as a function of $E_0\theta$, $E_0\theta^2$, and $E_0\theta^3$. The log scale underlines the exponential decay.

$-k_{\perp}$ to k_{\perp} [6–8], the W term inside the exponent is now W/N allowing a much larger coherence at comparable values of E_{\perp} . Reversely, this reduced decoherence allows large values of E_{\perp} , up to one eV for He, where attraction forces play a negligible role and where, due to small wavelength, the topological accuracy can be in the pm range [2,4]. The measured DWF decays exponentially both with increased collision energy and with increased angle of incidence, however, when plotted as a function of $E\theta^3$, the data recorded during an E_{scan} or a θ_{scan} tend to fall on top of each other as illustrated in Fig. 5. Figure 6

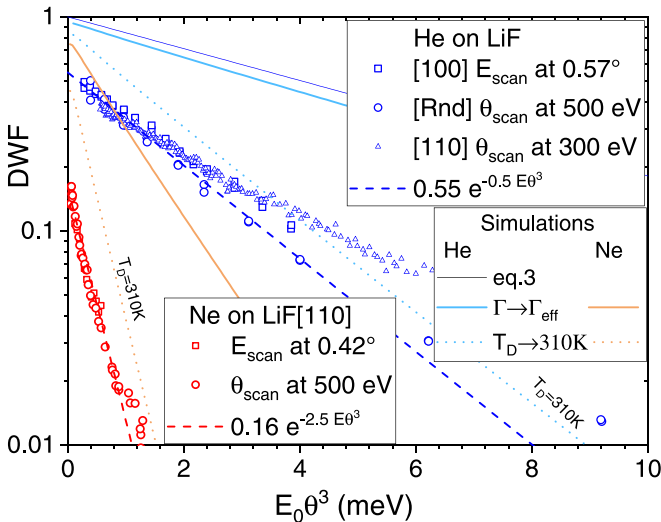


FIG. 6. The DWF, measured as the relative intensity of elastic diffraction, is reported for He and Ne projectiles on LiF along various orientations as a function of $E\theta^3$. The (\circ, \circ) symbols were recorded on the same surface and the associated dashed lines are only to guide the eye outlining the effect of the projectile mass on the decay constant. The (\triangle) symbols correspond to a different target suggesting a possible influence of the surface coherence length (defect density). The simulations are described in the discussion.

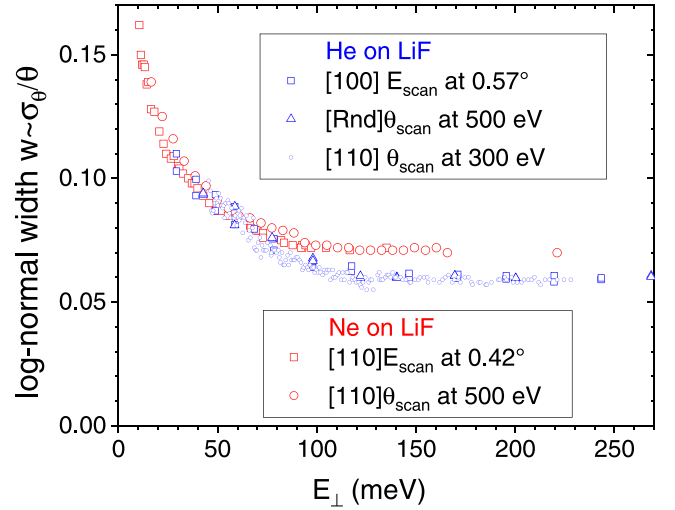


FIG. 7. The log-normal width $w \approx \sigma_{\theta}/\theta_{\text{scat}}$ of the inelastic scattering polar profile is reported as a function of the perpendicular energy E_{\perp} , for helium (\circ) and neon (\circ) atoms impinging on LiF under various conditions indicated in insets.

displays the DWF measured with helium and Ne projectiles in a wide variety of initial conditions as a function of $E\theta^3$. In spite of a significant scattering of the experimental points, partly due to different samples, a dominant exponential decay is observed. The corresponding prefactor and a decay rate are indicated in Fig. 6 and will be discussed later.

B. The elastic scattering width

For most of the systems investigated, the polar profile is well-fitted by the sum of log-normal profile and a Gaussian width σ_e identical to that of the primary beam. However, when the elastic ratio is less than a few percent, the elastic contribution is not clearly resolved, and we usually impose the elastic width used in the fit to be the same as that of the primary beam. It should be stated that sometimes, the direct beam, which is systematically recorded before or after target insertion, is better fitted by a non-Gaussian profile, in these cases, the same profile is used in the fitting deconvolution. In some cases, with our best angular resolution, there could be indications of a slight broadening at the base of the elastic peak as compared with the shape of the direct beam, but the effect could also be due to deformation of the inelastic profile that would be poorly described by a log-normal profile. This aspect is not important here and will not be discussed further.

C. The inelastic scattering width w of the log-normal inelastic profile

Figure 7 reports the evolution of the relative width of the polar profile measured with neon and helium projectile under various conditions of energy and angle on a LiF surface at room temperature. Here again, the data indicate that the polar relative width is not too sensitive to the crystallographic axis. When plotted as a function of the perpendicular energy E_{\perp} , the data reasonably align on each other irrespective of major differences in the Debye-Waller factor and of the absolute magnitude of the measured standard deviation σ_{θ} . The

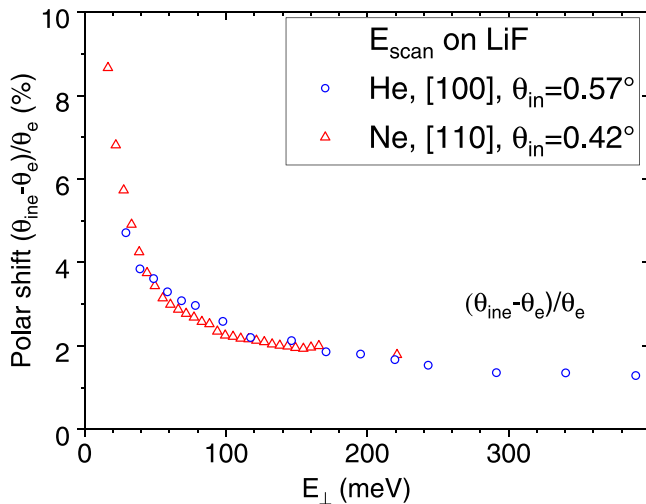


FIG. 8. The relative shift between the peak position of the elastic peak and the median value of the inelastic profile, as modeled in Fig. 2 is reported for helium and neon projectiles.

observed width seems to level at a fixed value for perpendicular energies larger than 100 meV and to increase significantly below. The data recorded with helium and neon appear rather similar, with a slightly different plateau value at large values of E_{\perp} . This rapid increase of the relative width starting at energies E_{\perp} much larger than the well depth D is at the heart of the present paper suggesting a new experimental approach to estimate the well-depth D from purely inelastic scattering profiles. This behavior was first identified in a recent paper devoted mainly to the elastic diffraction of neon atoms on a LiF surface [5] where a calculated [22] potential energy landscape could be optimized to data. Starting from these results a model analysis is developed in Sec. III D on a more general basis of Morse potentials. For helium, we use for the mean planar potential a well depth $D = 8.5$ meV from TEAS spin echo measurement [23] while for neon, we took the value of $D = 10.3$ meV derived in Ref. [5] slightly below the recommended value in Ref. [24].

D. The angular shift $\delta\theta$ between the elastic and inelastic polar profiles

The fitting procedure illustrated in Figs. 2 and 3 was first developed with a constraint forcing a common value for the center of the elastic and inelastic scattering profiles. The reduced number of free parameters was expected to ensure better stability. However, we rapidly identified situations where the fit is much better with an inelastic scattering profile located at slightly larger angles: $\theta_{ine} = \theta_s + \delta\theta$, with θ_s the specular angle and $\delta\theta \geq 0$. Figure 8 indicates that this shift increases rapidly below 100 meV. The shift is arbitrarily plotted relative to the elastic scattering angle, the absolute deviation is comparatively small. For instance, the shift does not exactly reach zero at large values of E_{\perp} obtained around 1–2° incidence, the value of 1–2% corresponds to only 0.004°, which could be affected by our angular resolution [4]. More relevant probably, as can be seen in Fig. 3, the fit is not perfect, leaving a clear residue in the rising and trailing edges indicat-

ing possible contributions from defects and/or from the fact that the log-normal profile used here is only an approximation as will be discussed in Secs. II B and IV. Figures 7 and 8 display the evolution of the inelastic scattering width σ_{θ} and shift $\delta\theta$ relative to the specular angle $\theta_e = 2\theta_i$ and have a comparable behavior.

Summarizing the experimental findings:

(i) The inelastic polar profile hardly depends on the crystallographic direction investigated (Fig. 4).

(ii) The Debye-Waller factor depends primarily on the reduced variable $E\theta^3$ (see Fig. 5).

(iii) The relative inelastic width σ_{θ}/θ_s , as measured by w in Eq. (1) in a log-normal fit, depends mainly on the perpendicular energy E_{\perp} . It appears stable above 100 meV but increases rapidly below (see Fig. 7).

(iv) The median position of the inelastic scattering polar scattering profile tends to become significantly over-specular at low values of E_{\perp} (see Fig. 8).

We now rapidly present a model developed to describe the inelastic scattering profiles in fast atom scattering at grazing incidence.

III. THEORETICAL CONSIDERATIONS

A. Elastic diffraction

The elastic diffraction corresponding to the bright spots on the Laue circle in Fig. 1 and Fig. 2(d) can be understood as the diffraction on a perfectly periodic ideal surface, i.e., with atoms frozen at equilibrium positions. It was soon realized experimentally [25] and theoretically [25–27] that, in GIFAD, there is a strong decoupling between the fast movement along the low index crystalline direction, almost parallel to the beam, and the much slower movement in the perpendicular (y, z) plane. In this plane the system is equivalent to a projectile with an energy E_{\perp} evolving in the 2D averaged potential energy landscape (PEL) $V_{\perp}(y, z) = \frac{1}{a} \int_0^{a_x} V(x, y, z) dx$, where a_x is a lattice parameter along x .

This decoupling, specific of grazing incidence was also observed at thermal energies when measured at comparatively grazing incidence [28]. It was investigated in detail theoretically [26,27] and qualitatively understood as due to a weak coupling combined with a comparatively large associated energy preventing possible transitions. The weak coupling is due to the obliquity factor [29,30] while the large energy associated to the exchange of a reciprocal lattice vector G_x along x is due to kinematic considerations, the projectile momentum k_x along x being orders of magnitude larger than G_x . It should be noted that with surface atoms frozen at the equilibrium position, even classical mechanics predicts extremely narrow polar scattering profiles, because the same obliquity factor governs the polar scattering width. In other words, the width of scattering profiles calculated from classical mechanics does not derive from the surface corrugation along x but is almost entirely due to the thermal motion of surface atoms [31–33].

This approach is known as the axial surface channeling approximation (ASCA) and is now very well established for fast atom elastic diffraction and also for classical atom scattering. Aside from the fact that the PEL investigated with GIFAD along a given direction is the 3D PEL averaged along

this direction, the information behind the elastic diffraction is equivalent to that derived from TEAS and similar theoretical models can be used to analyze the data.

Of course, even at zero temperature, the surface atoms are not standing still at equilibrium positions but quantum mechanics indicates that position and momentum cannot be treated as independent (see e.g., Ref. [34] for a ball hitting a harmonic oscillator). In single scattering conditions such as x-ray, TEAS, or neutron diffraction, the equilibrium position reappears because it is the only one where large scale coherence can build up. The intensity of the associated coherent scattering is simply the phase coherence resulting from an ensemble of thermally displaced surface atoms $DWF = e^{-\delta k^2 \sigma_z^2}$ where $\sigma_z^2(T) = \langle u_z^2 \rangle_T = \frac{3\hbar^2}{2Mk_B T_D} \coth \frac{T_D}{2T}$ is the variance of the thermal displacement of surface atoms in the z direction. In a harmonic model, it is derived directly from the Debye frequency ω_D of the local harmonic oscillator describing a surface atom, also described by the Debye temperature via the Boltzmann constant $k_B T_D = \hbar \omega_D$. Elastic diffraction nicely captures the ultimate structural information, which is the equilibrium position but the counterpart is that it does not contain any direct information on the collision between the projectile and surface target atoms, which govern the momentum transfer. With the rigid lattice used above and the repulsive mean planar potential of Sec. I, the trajectory is analytic and these binary momentum exchanges can be calculated giving rise to the specular reflection of the projectile and to recoil momentum to each encountered surface atom. The classical energy loss ΔE_{Cl} is the sum of the recoil energies of the surface atoms [7,8]

$$\Delta E_{Cl} = \frac{2}{3} \mu E \Gamma a \theta_i^3 \equiv N E_r = N \mu E (2\theta_i/N)^2, \quad (2)$$

where μ is the projectile to target mass ratio and can be used to define $N = 6/(\Gamma a \theta_i)$, the mean number of equivalent binary collisions producing the same energy loss. The last term is N times the binary recoil energy E_r resulting from each individual deflection by $2\theta_{in}/N$. The DWF adapted to grazing incidence is now

$$DWF = \exp\left(-\frac{3\Delta E_{Cl}}{\hbar \omega_D} \coth \frac{T_D}{2T}\right). \quad (3)$$

B. Inelastic diffraction, the surface stiffness Γ

Aside from the probability (DWF), let us focus on a fundamental difference of the inelastic collision in TEAS and GIFAD. During a head-on collision at hyper-thermal energy, all the projectile momentum is reversed independently from the fact that the surface atom is protruding or recessing from the mean surface plane. At variance, under grazing incidence, the distance of closest approach, and therefore the magnitude of the momentum transfer will be directly affected by this departure from equilibrium. At grazing incidence, the binary collision approximation where the overall momentum transfer is decomposed in terms of successive binary collisions with the closest surface atoms is still relevant due to the exponential character of the repulsive forces [8]. The momentum transfer can be evaluated from a straight line approximation [35] with a projectile flying at a distance z_r above the surface and, for a purely repulsive binary potential such as $V(z) \propto e^{-\Gamma z}$, the

scattering angle also depends exponentially on the closest distance between the projectile and the surface atom. As a result of a surface atom protruding or receding by $\pm dz$ is scattered at angles $\theta_{\pm} \propto e^{-\Gamma(z_r \pm dz)}$. Considering $dz = \sigma_z(T)$ as the standard deviation of Gaussian atomic displacement defined above, the scattering distribution due to this single collision is a log-normal distribution where the specular angle corresponding to the equilibrium position is the median value while the relative width is $w = \Gamma \sigma_z(T)$ [7,8].

The stiffness Γ is not an abstract concept but a physical parameter describing the decay of the surface electron density. For all quantum systems the Schrodinger equation indicates that, in regions where the electron potential energy is much less than the binding energy I_p , the electron wave function should decay exponentially with the distance. Far from the bulk, the surface electronic density should then decay as $\Psi(z)^2 \propto e^{-\Gamma z}$ with $\Gamma \approx 2\sqrt{2I_p}$ where I_p is here the binding energy of the valence electrons, the LiF work function. For a compact atom such as helium or neon with tightly bound electrons, the Pauli repulsion at a distance z from the bulk is also expected to be proportional to the surface electronic density. Depending on whether we consider the top or mean value of the valence band I_p should be 11.3 eV [36] to 13 eV [37] yielding values of Γ between 3.4 and 3.7 \AA^{-1} inline with recent theoretical and experimental works [5,22].

Both He and Ne have much larger binding energy than LiF so that most of the energy variation when approaching the surface should be related to the deformation of the Fluorine atoms. He and Ne are therefore expected to have a similar decay rate of the mean planar potential, and only the absolute magnitude of the repulsive term should be larger for neon, which has more outer electrons.

Since the valence band is located on F^- ions, the Li^+ play a limited role in the momentum transfer associated to diffraction, as confirmed by trajectory simulations [38].

Note that the simple relation $w = \Gamma \sigma_z$ holds only for a single scattering event. The overall elastic scattering probability is the product of all the individual elastic probabilities but the overall inelastic scattering profile, depends on how many individual inelastic events contribute to the polar inelastic profile.

C. Statistics of inelastic events

As a handy simplification, one can assume that the specular deflection is due to N equivalent binary collisions, i.e., replacing the quasi-Gaussian probability distribution (Eq. (5) in Ref. [8]) with a square probability distribution. Mathematically, the convolution of N log-normal distributions is not a log-normal distribution, however, for comparatively small values of $w \approx \sigma_{\theta}/\theta_e = \sigma_{\theta}/2\theta_i \leq 0.1$, the property is numerically well verified [8] and, for N identical deflections, the resulting relative width parameter is reduced by \sqrt{N} indicating simply that the final variance is the sum of individual variances. We note that Eq. (2) can be written as $\Delta E_{Cl} = 4\mu E \theta_{in}^2/N$ where $4\mu E \theta_{in}^2$ is the energy loss that would arise if only one atom would deflect the projectile by $2\theta_i$. The number $N = \frac{6}{\Gamma a \theta_{in}}$ is hence well-defined and interpreted as the mean number of collisions, each deflecting the projectile by $d\theta_1 = 2\theta_{in}/N$ with an associated recoil energy, $E_r = \mu E d\theta_1^2$ so that $\Delta E_{Cl} = N E_r$.

The statistics is then easily expanded in terms of the number n of inelastic collisions

$$P(n) = \binom{N}{n} p_e^{N-n} (1-p_e)^n / (1-p_e^N), \quad (4)$$

where the last term is here to normalise among the inelastic events only. The final variance $\sigma_{\theta_f}^2$ can be evaluated from the variance $\sigma_{\theta_i}^2 = (d\theta_1 \Gamma \sigma_z)^2 \approx (\theta_{in}^2 \Gamma^2 a \sigma_z / 3)^2$ of an individual inelastic collision:

$$\begin{aligned} (a) \quad & \sigma_{\theta_f}^2 = \sum_n P(n) n \sigma_{\theta_i}^2 \\ (b) \quad & \text{for } p_e \approx 0, \quad \sigma_{\theta_f}^2 \approx \sigma_{Cl}^2 = N \sigma_{\theta_i}^2 = \frac{2a}{3} \theta_{in}^3 \Gamma^3 \sigma_z^2 \\ (c) \quad & \text{for } p_e \approx 1, \quad \sigma_{\theta_f}^2 \approx \sigma_{Qu}^2 = \sigma_{\theta_i}^2 = \frac{a^2}{9} \theta_{in}^4 \Gamma^4 \sigma_z^2 \end{aligned} \quad (5)$$

The limiting cases are given by the classical limit σ_{Cl} where all collisions are inelastic and the quasiquantum limit σ_{Qu} where inelastic events (trajectories) are dominated by a single inelastic collision.

Both predictions indicate that the measured relative width $w \approx \sigma_{\theta_f} / 2\theta_i$ should decrease at small angle of incidence during a θ_{scan} or stay constant during an E_{scan} . In this latter case, the angle of incidence is fixed and increasing E_{\perp} only brings the trajectory closer to the surface but does not change its shape nor the number of collisions or their relative strength $\delta k_z / k_x$ so that the relative width w should stay fixed.

This simple description of the scattering width as a perturbative broadening of the elastic scattering from an ideal surface with atom fixed at equilibrium positions was developed as the quantum binary collision model (QBCM) [8]. We suggest in the next sections, that the purely repulsive approach is too restrictive, much more than it is in TEAS where the most important correction, known as the Beeby correction is assumed to be qualitatively important only for values of $E_{\perp} \sim D$.

D. The attractive forces, the effective stiffness Γ_{eff}

The main properties of the QBCM described above derive from the exponential form of the repulsive part of the interaction and could remain valid after adding a weak attractive part. These are the polarization forces due to the Madelung electric field of the LiF surface, which should also exhibit exponential decay with a typical range on the order of the lattice unit and the van der Waals forces, which should have a polynomial form (see e.g., Ref. [39] for a recent discussion in noble gas dimers). The resulting physisorption well can host bound states resonances whose exact locations are sensitive to both sides of the trapping well. These can be observed in GIFAD [40] but the TEAS has demonstrated exceptional resolution [23] (or [41] for a recent review) providing a challenging description of the attractive part.

Here, the width of the polar profile originates from the part of the trajectory close to the surface and is expected to be sensitive mainly to the shape of the repulsive wall. We decided to use an exponential form also for the attractive part because of its simple form and analytic properties. We choose a Morse potential of the form

$$V_M(z) = D e^{-\Gamma(z-z_0)} - 2D e^{-(\Gamma/2)(z-z_0)} \quad (6)$$

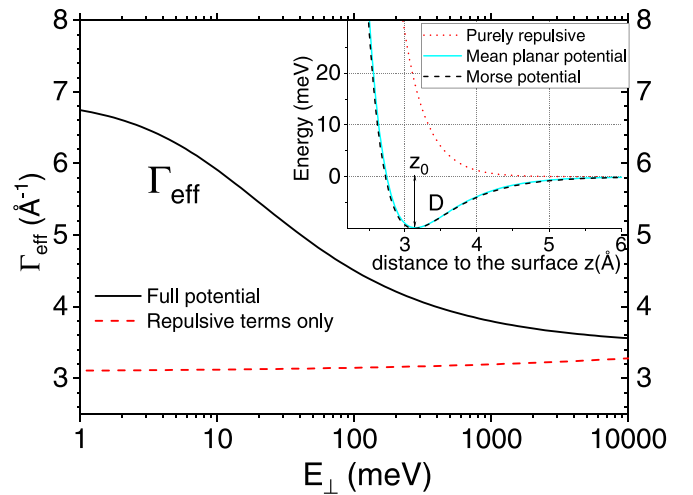


FIG. 9. The mean interaction potential for Ne-LiF from Ref. [5] is reported in the insert together with the fitted Morse potential. The logarithmic derivative $\Gamma_{eff} = -V'(z)/(V(z) + D)$ is expressed as a function of the energy E_{\perp} (see text).

where the attractive part has a decay range twice larger than the repulsive one. Compared with the pure repulsive potential where only Γ was found important, two additional parameters are needed: the well depth D and the equilibrium distance z_0 . Using Eq. (6), the turning point z_t when an atom of energy $E_{\perp} = V_M(z_t)$ bounces back from the surface is given by

$$z_t = z_0 - \frac{2}{\Gamma} \ln \left(1 + \sqrt{1 + \frac{E_{\perp}}{D}} \right) \quad (7)$$

The parameters $\Gamma = 3.46 \text{ \AA}^{-1}$, $D = 10.3 \text{ meV}$, and $z_0 = 3.13 \text{ \AA}$ have been fitted to the *ab initio* potential energy landscape calculated in Ref. [22] and optimized to elastic diffraction data with a fast quantum scattering code for the Ne-LiF system for E_{\perp} ranging between 20 and 200 meV [5]. Both the empirically adjusted mean planar potential and the Morse potential used hereafter are displayed in the inset of Fig. 9.

Rather than a direct evaluation of the momentum transfer along the projectile trajectory, we compare in Fig. 10 neon data recorded during an E_{scan} with prediction using the QBCM and the Morse potential. We first recall that, for an E_{scan} and a purely repulsive potential, the classical limit of Eq. (5) predicts a constant value of the log-normal width w , as illustrated by the horizontal dotted line in Fig. 10 corresponding to neon atoms at $\theta_{in} = 0.42^\circ$ [5]. To better illustrate the role of the attractive forces we have tried to evaluate its contributions on three separated parts of the atom trajectory, (i) the way in of the trajectory, (ii) the comparatively closer collisions with surface atoms, and (iii) the way out.

(i) The modification of the perpendicular energy before the impact on the surface ($\infty > z \geq z_0$).

This correction corresponds to the well-known Beeby correction factor [42] widely used in TEAS [43]. It considers that the attractive part of the mean planar potential has the effect of changing the effective perpendicular kinetic energy before the projectile evolution on the repulsive wall. The Beeby correction considers that elastic diffraction probability

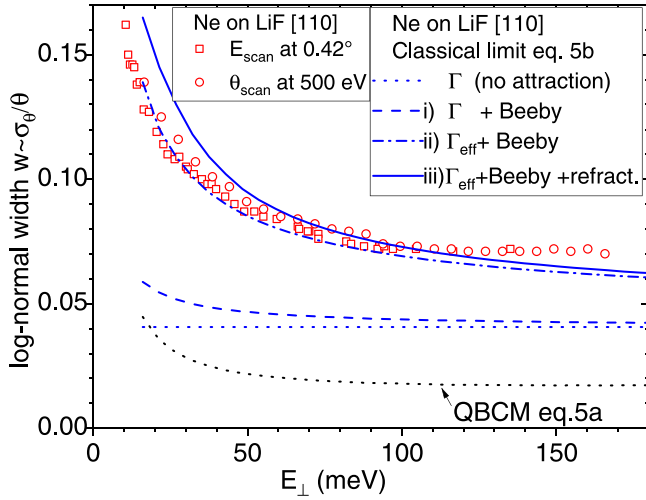


FIG. 10. The log-normal relative width $w \approx \sigma_\theta / \theta_{scat}$ of the inelastic scattering polar profile is reported for conditions indicated on the left inset. To outline the different contributions, incomplete models are presented and discussed in the text.

can be evaluated as that of a particle with an effective energy $E'_\perp = E_\perp + D$.

For grazing incidences, the situation is similar to the image charge acceleration increasing the impact energy of ions before impact on a surface [44,45] and it is usually modeled as an effective angle of incidence $\theta_{\text{eff}} = \sqrt{\theta_i^2 + D/E}$ providing the same impact energy $E_\perp + D$. The polar straggling $\sigma_\theta = w \times \theta_{\text{eff}}$ acquired at impact should be preserved so that the relative width is now $w' \approx w \times \theta_{\text{eff}} / \theta_i$. The corresponding dashed line in Fig. 10 indicates a moderate increase of w at low values of E_\perp but only for values of E_\perp close to D . The value of $\sigma_z = 0.098 \text{ \AA}$ considered here for data recorded at 300 K, is taken from *ab initio* extensive calculations [2,18] of the LiF crystal and corresponds to a Debye temperature $T_D = 550 \text{ K}$ at the surface, very close to the recommended value derived from TEAS measurements [46].

(ii) The modification of the stiffness of the surface at the moment of impact ($z < z_0$).

We now take into account that the actual stiffness at the moment of impact is not Γ that of the sole repulsive term of the potential but the logarithmic derivative $-V'/V$ of the actual potential combining repulsive and attractive part at the turning point. More precisely, taking into account the above Beeby correction that the effective energy is $E_\perp + D$, the effective stiffness is defined as $\Gamma_{\text{eff}} = -V'/(E_\perp + D)$, which remains well-defined even for low values of E_\perp . Using the Morse potential $V_M(z)$ from Eq. (6) as a mean planar potential, the effective stiffness of the repulsive wall is given by

$$\Gamma_{\text{eff}}(z) = \Gamma \left[1 + \left(1 + \frac{E_\perp}{D} \right)^{-1/2} \right] \quad (8)$$

Figure 9 reports the evolution of the effective stiffness with the energy E_\perp and shows an increase, which is maximum at low values but remains significant above 100 meV. The dashed-dot line in Fig. 10 now shows a sharp increase of w also starting at perpendicular energies around 100 meV.

(iii) The refraction of the atoms inelastically scattered when leaving the surface ($z_0 \leq z < \infty$)

This last contribution is the reverse transformation of (i). When climbing the attractive branch of the mean planar potential, the particles scattered from the surface at an angle θ_{emi} will give back the energy D along the z direction so that the observation angle is $\theta_{\text{obs}} = \sqrt{\theta_{\text{emi}}^2 - D/E}$. The median value θ_{emi} of the log-normal scattering profile is restored at the specular angle, however the associated Jacobian $J = d\theta_{\text{obs}}/d\theta_{\text{emi}}$ induces a nonlinear stretching of the log-normal distribution at low scattering angles. The effect on the scattering profile was estimated by fitting the resulting scattering profile by a log-normal distribution to produce a relative width w and correspond to the full line in Fig. 10.

The sharp increase is qualitatively well reproduced a dominant contribution coming from the account of Γ_{eff} in Eq. (8). The agreement with the observation seems better for the classical limit, as if a single inelastic collision (among N) is enough to induce a fully classical behavior. This quantitative agreement should not be overestimated because, as will be discussed below, a proper account of phonons can probably affect the absolute magnitude. However, we consider that the influence of the well depth D to the effective stiffness Γ_{eff} is a very robust effect, which has to be taken into account to estimate the polar width. It is the main finding of the present paper. Note that in TEAS, using diffracted intensities recorded between 17 and 270 meV on a Ni(110) surface, a mean potential energy curve could be extracted indicating a similar twofold increase of the surface stiffness at low energy [47].

The consequence of the well depth D on the Debye-Waller factor is less quantitative. Taking into account the attractive terms, the DWF in Eq. (3) can be written using the classical energy loss of Eq. (2) but evaluated with the effective stiffness Γ_{eff} and effective angle of incidence θ_{eff} defined above. The result reported in Fig. 6 as full lines in light blue or orange indicates that neither the offset nor the slope is well reproduced and the improvement compared with the purely repulsive form is only marginal. This is quite different from TEAS where the Beeby correction is widely used to adapt the Debye-Waller factor to measurements [42,48]. In particular it is responsible for a significant offset at very low impact energy. In GIFAD, changing θ to θ_{eff} increases the impact energy but the angle remains grazing so that the momentum is still shared among several surface atoms with a limited consequences on the Debye-Waller factor. The situation is even worse concerning the angular shift in Fig. 8, the asymmetric stretching of the polar profile on the way out produces a shift that is much less than the one observed and tends to decrease the mean inelastic polar profile. These discrepancies are discussed in the next section.

IV. DISCUSSION

The similarities between Fig. 7 and Fig. 8 suggest that a common origin could explain both behaviors but this is not confirmed by our simulations. A possible explanation could be related to the reduction of the surface reflectivity at the most grazing incidences. One important aspect of

grazing angle collision is the sensitivity to the presence of obstacles such as ad-atoms or step edges etc. These are becoming increasingly important as the angle of incidence is decreased and their influence can be measured by the reflectivity, the ratio of reflected particles intensity related to that of the primary beam before target insertion. Below one deg of incidence, this reflectivity becomes difficult to measure because, events with a beam diameter \varnothing below $100\ \mu\text{m}$, the length of the zone illuminated $\sim \varnothing/\theta_{\text{in}}$ becomes larger than the typically crystal dimension around 10 mm. However, this restriction alone does not explain that the lowest possible incidence is usually limited by the surface quality. We observed optimum reflectivity with large wafers and freshly grown layers of semiconductor directly measured inside the molecular beam epitaxy chamber [3]. During growth, it was then possible to measure the influence of incomplete layers on the inelastic scattering angle [49]. In the present case, even with freshly cleaved LiF surfaces (see Acknowledgments) the observed reflectivity usually drops drastically below a few percent for incidence angles below 0.3° . This dependency maybe of limited importance for elastic diffraction, which is spot-like and cannot be deformed but the inelastic scattering profile is probably affected since particles scattered under-specular have less chances to reach the detector without encountering an obstacle and the observed tendency of over-specular reflection observed in Fig. 8 could simply reflect the reduced probability for particle scattered under-specular to reach the detector. The effect would probably reduce the measured inelastic intensity and its width at the lowest incidences, and therefore also affect the Debye-Waller factor but probably only by a few percent as suggested by the effect on the mean position of the inelastic polar profile.

The disagreement between the measured and predicted Debye-Waller factor is probably more indicative of a lack in the model. A major weakness of the QBCM is that surface vibration are treated only through the local Debye oscillator thus neglecting the phonons mode, which are the genuine eigenstates of vibrations at surfaces. Only few authors have developed approaches where phonons are explicit, most are adapted to TEAS [34,50–52] but also to grazing incidences [53,54].

In GIFAD, the successive momentum transfer to the surface atoms occur in a timescale $\tau = 1/\Gamma v_{\perp}$ with $v_{\perp} = \sqrt{2E_{\perp}/m_p}$ much shorter than the vibration time so that momentum transfer along the N successive collisions of the trajectory should be coherent, exciting preferentially transverse phonons having a wavelength close to $N \cdot a \sim 6/\Gamma\theta$. Since the interaction with Fluorine ions dominates, the vector of exchanged momentum should decompose with almost equal weight to acoustic and optical surface phonons, the former having associated low energy while the second should have flat dispersion curves with an energy close to the high-frequency limit of the Debye oscillator considered here. The model described above does not take phonons into account and the easiest way to improve the agreement with data is to reduce the Debye temperature to 310 K (which also provided a better qualitative agreement in Ref. [8]). The associated prediction of the DWF is depicted by dotted lines in Fig. 6 and is much closer to the experimental data with slopes, which now

compares to the measured ones. This low value of the Debye temperature is probably not a good description of amplitude of the thermal displacement but should be considered as an indication that low energy phonons can contribute to GIFAD [53] and deserves deeper investigations.

V. CONCLUSIONS

We have presented measurements of the polar scattering profile of fast helium and neon atoms with energies ranging from 0.2 keV to 5 keV diffracted at the surface of a LiF single crystal under grazing incidence. These profiles were found to be independent on the crystallographic axis probed by the primary atomic beam. The fit of the inelastic profile by a log-normal function provides an estimate of the DWF, which is found to depend on $E\theta_{\text{in}}^3$, a quantity proportional to the classical energy loss in Eq. (2) as suggested in [7,8]. The relative width w derived from the log-normal fit is found to depend primarily on the energy $E_{\perp} \sim E\theta_{\text{in}}^2$, i.e., for a given system projectile-surface, on the distance of closest approach. The value of w is found stable for larger than 100 meV but increases rapidly below. Both He and Ne projectiles display comparable values and similar behavior. Using a Morse potential fitted to a potential energy landscape previously adjusted to elastic diffraction data and a binary collision model together with a well-accepted value of the Debye temperature, the sharp increase of w is well reproduced and the analysis suggests a dominant role of the effective stiffness $-V'/(E_{\perp} + D)$ at the distance of closest approach.

To our knowledge, this rather simple effect was not documented so far, but a quick look at the inset of Fig. 9 indicates that the mean planar potential is seriously affected by the attractive forces. The repulsive wall is brought significantly closer to the surface and, consistently it has to grow at a faster rate to merge with the high energy values (low z) where the attraction is usually neglected. Our work suggests that under grazing incidence specific phonon mode may participate to the inelastic scattering, which takes place on a relatively long distance $L \sim 6/\Gamma\theta$ (typically around $\sim 100\ \text{\AA}$ for $\theta = 1^\circ$) and where all surface atoms receive a momentum coherently oriented towards the bulk. In the present form, a specific Debye temperature almost twice as low as the one derived from TEAS was found to improve the description of the DWF. The much weaker effect of angular shift between elastic and inelastic profile was not reproduced in our model and could be due to surface defects.

To first order, elastic diffraction is qualitatively well described by a hard corrugated wall model where the surface is modeled as an infinitely hard surface. We show here that, its counterpart, the inelastic polar profile is mainly sensitive to the stiffness Γ_{eff} of the hard-wall and that this later is very sensitive to the attractive forces. The method can probably be applied to estimate the physisorption well for heavier elements were the diffraction features are more difficult to obtain and were attractive forces can be larger.

ACKNOWLEDGMENT

We are grateful to Hynd Remita for the irradiation of the LiF samples by γ rays from the Cobalt source of the

Institut de Chimie Physique at Orsay, favoring further cleaving with large terraces. This work received support from

LabEx PALM (ANR-10-LABX-0039-PALM) and Chinese Scholarship Council (CSC) Grant No. 201806180025.

- [1] P. Atkinson, M. Eddrief, V. H. Etgens, H. Khemliche, M. Debiossac, A. Momeni, M. Mulier, B. Lalmi, and P. Roncin, Dynamic grazing incidence fast atom diffraction during molecular beam epitaxial growth of GaAs, *Appl. Phys. Lett.* **105**, 021602 (2014).
- [2] A. Schüller, S. Wethekam, D. Blauth, H. Winter, F. Aigner, N. Simonović, B. Solleder, J. Burgdörfer, and L. Wirtz, Rumpling of LiF(001) surface from fast atom diffraction, *Phys. Rev. A* **82**, 062902 (2010).
- [3] M. Debiossac, A. Zugarramurdi, H. Khemliche, P. Roncin, A. G. Borisov, A. Momeni, P. Atkinson, M. Eddrief, F. Finocchi, and V. H. Etgens, Combined experimental and theoretical study of fast atom diffraction on the $\beta_2(2 \times 4)$ reconstructed GaAs(001) surface, *Phys. Rev. B* **90**, 155308 (2014).
- [4] M. Debiossac, P. Pan, and P. Roncin, Grazing incidence fast atom diffraction, similarities and differences with thermal energy atom scattering (TEAS), *Phys. Chem. Chem. Phys.* **23**, 7615 (2021).
- [5] M. Debiossac, P. Roncin, and A. G. Borisov, Refraction of fast Ne atoms in the attractive well of a LiF(001) surface, *J. Phys. Chem. Lett.* **11**, 4564 (2020).
- [6] P. Rousseau, H. Khemliche, N. Bundaleski, P. Soullisse, A. Momeni, and P. Roncin, Surface analysis with grazing incidence fast atom diffraction (GIFAD), *J. Phys.: Conf. Ser.* **133**, 012013 (2008).
- [7] J. R. Manson, H. Khemliche, and P. Roncin, Theory of grazing incidence diffraction of fast atoms and molecules from surfaces, *Phys. Rev. B* **78**, 155408 (2008).
- [8] P. Roncin and M. Debiossac, Elastic and inelastic diffraction of fast atoms, Debye-Waller factor, and Mössbauer-Lamb-Dicke regime, *Phys. Rev. B* **96**, 035415 (2017).
- [9] H. Winter and A. Schüller, Fast atom diffraction during grazing scattering from surfaces, *Prog. Surf. Sci.* **86**, 169 (2011).
- [10] V. A. Morosov, A. Kalinin, Z. Szilagyí, M. Barat, and P. Roncin, 2π spectrometer: A new apparatus for the investigation of ion surface interaction, *Rev. Sci. Instrum.* **67**, 2163 (1996).
- [11] S. Lupone, S. Damoy, A. Hussein, N. Briand, M. Debiossac, S. Tall, and P. Roncin, Note: A large open ratio, time, and position sensitive detector for time of flight measurements in UHV, *Rev. Sci. Instrum.* **86**, 126115 (2015).
- [12] J. S. Lapington, A comparison of readout techniques for high-resolution imaging with microchannel plate detectors, *Nucl. Instrum. Methods Phys. Res. A* **525**, 361 (2004).
- [13] M. Debiossac and P. Roncin, Image processing for grazing incidence fast atom diffraction, *Nucl. Instrum. Methods Phys. Res. B* **382**, 36 (2016).
- [14] J. Villette, Etude expérimentale de l'interaction rasante d'atomes et d'ions sur des surfaces isolantes, Ph.D. thesis, Université Paris sud-XI, 2000.
- [15] J. Villette, A. G. Borisov, H. Khemliche, A. Momeni, and P. Roncin, Subsurface-Channeling-Like Energy Loss Structure of the Skipping Motion on an Ionic Crystal, *Phys. Rev. Lett.* **85**, 3137 (2000).
- [16] H. Khemliche, J. Villette, A. G. Borisov, A. Momeni, and P. Roncin, Electron Bihole Complex Formation in Neutralization of Ne^+ on LiF(001), *Phys. Rev. Lett.* **86**, 5699 (2001).
- [17] F. Aigner, N. Simonović, B. Solleder, L. Wirtz, and J. Burgdörfer, Suppression of Decoherence in Fast-Atom Diffraction at Surfaces, *Phys. Rev. Lett.* **101**, 253201 (2008).
- [18] L. Frisco and M. S. Gravielle, Thermal effects on helium scattering from LiF(001) at grazing incidence, *Phys. Rev. A* **102**, 062821 (2020).
- [19] R. Pfandzelter, Effects of defect structures at surfaces and thin films on grazing scattering of fast ions, *Phys. Rev. B* **57**, 15496 (1998).
- [20] J. Seifert, J. Lienemann, A. Schüller, and H. Winter, Studies on coherence and decoherence in fast atom diffraction, *Nucl. Instrum. Methods Phys. Res. B* **350**, 99 (2015).
- [21] D. Farías and K. H. Rieder, Atomic beam diffraction from solid surfaces, *Rep. Prog. Phys.* **61**, 1575 (1998).
- [22] J. E. Miraglia and M. S. Gravielle, Reexamination of the interaction of atoms with a LiF(001) surface, *Phys. Rev. A* **95**, 022710 (2017).
- [23] D. J. Riley, A. P. Jardine, S. Dworski, G. Alexandrowicz, P. Fouquet, J. Ellis, and W. Allison, A refined He–LiF(001) potential from selective adsorption resonances measured with high-resolution helium spin-echo spectroscopy, *J. Chem. Phys.* **126**, 104702 (2007).
- [24] G. Vidali, G. Ihm, H.-Y. Kim, and M. W. Cole, Potentials of physical adsorption, *Surf. Sci. Rep.* **12**, 135 (1991).
- [25] P. Rousseau, H. Khemliche, A. G. Borisov, and P. Roncin, Quantum Scattering of Fast Atoms and Molecules on Surfaces, *Phys. Rev. Lett.* **98**, 016104 (2007).
- [26] A. Zugarramurdi and A. G. Borisov, Transition from fast to slow atom diffraction, *Phys. Rev. A* **86**, 062903 (2012).
- [27] A. S. Muzas, F. Gatti, F. Martín, and C. Díaz, Diffraction of h from LiF(001): From slow normal incidence to fast grazing incidence, *Nucl. Instrum. Methods Phys. Res. B* **382**, 49 (2016).
- [28] D. Farías, C. Díaz, P. Nieto, A. Salin, and F. Martín, Pronounced out-of-plane diffraction of H_2 molecules from a Pd(111) surface, *Chem. Phys. Lett.* **390**, 250 (2004).
- [29] C. Henkel, J.-Y. Courtois, and A. Aspect, Atomic diffraction by a thin phase grating, *J. Phys. II (France)* **4**, 1955 (1994).
- [30] M. Debiossac and P. Roncin, Atomic diffraction under oblique incidence: An analytical expression, *Phys. Rev. A* **90**, 054701 (2014).
- [31] D. M. Danailov and D. S. Karpuzov, Total reflection of energetic ions from crystal surfaces at glancing incidence, *Can. J. Phys.* **75**, 197 (1997).
- [32] D. M. Danailov, R. Pfandzelter, T. Igel, H. Winter, and K. Gärtner, Test of the interatomic potential in the eV-region by glancing-angle scattering of he-atoms from Fe(0 0 1), *Appl. Surf. Sci.* **171**, 113 (2001).
- [33] D. M. Danailov, Angular spectra of rainbow scattering at glancing kev He+ bombardment of NiAl(100) surface with

- transverse energies in the range 1–10 eV, *Nucl. Instrum. Methods Phys. Res. B* **264**, 29 (2007).
- [34] M. C. Schram and E. J. Heller, Hitting a ball on a spring: A simple model for understanding decoherence with wavefunctions, *Eur. J. Phys.* **41**, 025401 (2020).
- [35] M. S. Gravielle and J. E. Miraglia, Quantum interference in grazing scattering of swift He atoms from LiF(001) surfaces: Surface eikonal approximation, *Nucl. Instrum. Methods Phys. Res. B* **267**, 610 (2009).
- [36] J. Berkowitz, H. A. Tasman, and W. A. Chupka, Double-oven experiments with lithium halide vapors, *J. Chem. Phys.* **36**, 2170 (1962).
- [37] P. Roncin, J. Villette, J. P. Atanas, and H. Khemliche, Energy Loss of Low Energy Protons on LiF(100): Surface Excitation and H^- Mediated Electron Emission, *Phys. Rev. Lett.* **83**, 864 (1999).
- [38] P. Roncin, M. Debiossac, H. Oueslati, and F. Raouafi, Energy loss and inelastic diffraction of fast atoms at grazing incidence, *Nucl. Instrum. Methods Phys. Res. B* **427**, 100 (2018).
- [39] X. Sheng, J. Peter Toennies, and K. T. Tang, Conformal Analytical Potential for all the Rare Gas Dimers Over the Full Range of Internuclear Distances, *Phys. Rev. Lett.* **125**, 253402 (2020).
- [40] M. Debiossac, A. Zugarramurdi, P. Lunca-Popa, A. Momeni, H. Khemliche, A. G. Borisov, and P. Roncin, Transient Quantum Trapping of Fast Atoms at Surfaces, *Phys. Rev. Lett.* **112**, 023203 (2014).
- [41] A. Tamtögl, A. Ruckhofer, D. Campi, W. Allison, and W. E. Ernst, Atom-surface van der Waals potentials of topological insulators and semimetals from scattering measurements, *Phys. Chem. Chem. Phys.* **23**, 7637 (2021).
- [42] J. L. Beeby, The scattering of helium atoms from surfaces, *J. Phys. C: Solid State Phys.* **4**, L359 (1971).
- [43] A. A. Taleb, G. Anemone, L. Zhou, H. Guo, and D. Farías, Diffraction of CH_4 from a metal surface, *J. Phys. Chem. Lett.* **10**, 1574 (2019).
- [44] H. Winter, Image charge effects in ion surface scattering, *J. Phys.: Condens. Matter* **8**, 10149 (1996).
- [45] A. Arnau, F. Aumayr, P. M. Echenique, M. Grether, W. Heiland, J. Limburg, R. Morgenstern, P. Roncin, S. Schippers, R. Schuch, N. Stolterfoht, P. Varga, T. J. M. Zouros, and H. P. Winter, Interaction of slow multicharged ions with solid surfaces, *Surf. Sci. Rep.* **27**, 113 (1997).
- [46] H. Hoinkes, H. Nahr, and H. Wilsch, Surface Debye temperature by atomic beam scattering, *Surf. Sci.* **33**, 516 (1972).
- [47] K. H. Rieder and N. Garcia, Energy Dependence and Softness of the Potential for He Scattering from Ni(110), *Phys. Rev. Lett.* **49**, 43 (1982).
- [48] A. Politano, B. Borca, M. Minniti, J. J. Hinarejos, A. L. Vázquez de Parga, D. Fariás, and R. Miranda, Helium reflectivity and Debye temperature of graphene grown epitaxially on Ru(0001), *Phys. Rev. B* **84**, 035450 (2011).
- [49] M. Debiossac, P. Atkinson, A. Zugarramurdi, M. Eddrief, F. Finocchi, V. H. Etgens, A. Momeni, H. Khemliche, A. G. Borisov, and P. Roncin, Fast atom diffraction inside a molecular beam epitaxy chamber, a rich combination, *Appl. Surf. Sci.* **391**, 53 (2017).
- [50] G. Benedek, J. P. Toennies, and R. B. Doak, Surface-phonon spectroscopy of LiF(001) by inelastic scattering of He atoms: Theory and interpretation of time-of-flight spectra, *Phys. Rev. B* **28**, 7277 (1983).
- [51] S. Miret-Artés, Resonant inelastic scattering of atoms from surfaces, *Surf. Sci.* **339**, 205 (1995).
- [52] G. Benedek, S. Miret-Artés, J. P. Toennies, and J. R. Manson, Electron-phonon coupling constant of metallic overlayers from specular He atom scattering, *J. Phys. Chem. Lett.* **9**, 76 (2018).
- [53] M. C. Schram and E. J. Heller, Approach to coherent interference fringes in helium-surface scattering, *Phys. Rev. A* **98**, 022137 (2018).
- [54] L. Frisco and M. S. Gravielle, Phonon contribution in grazing-incidence fast atom diffraction from insulator surfaces, *Phys. Rev. A* **100**, 062703 (2019).